Research Square

Preprints are preliminary reports that have not undergone peer review.
They should not be considered conclusive, used to inform clinical practice,
or referenced by the media as validated information.

Application of an MRI-Visible Nanoparticle in the Treatment of Acute Liver Injury in Rats

Xiaojing Liu
The Affiliated Hospital of Qingdao University
Xiaomin Duan
The Affiliated Hospital of Qingdao University
Xiaoyuan Zhou
The Affiliated Hospital of Qingdao University
Zhiming Li
zhimingLee@yeah.net

The Affiliated Hospital of Qingdao University

Research Article

Keywords: Acute liver injury, Magnetic resonance imaging, Nanoparticles, Oxidative stress

Posted Date: November 17th, 2026

DOI: https://doi.org/10.21203/rs.3.rs-11143492/v1

License: This work is licensed under a Creative Commons Attribution 4.0 International License.
Read Full License

Application of an MRI-Visible Nanoparticle in the Treatment of Acute Liver Injury in Rats

Xiaojing Liu, Ms.[1†], Xiaomin Duan, MS[1†]. Xiaoyuan Zhou, Ms[1†], Zhiming Li, MD[1✉]

1 Department of Radiology, The Affiliated Hospital of Qingdao University, Qingdao, China.

✉**Corresponding Author:**
Zhiming Li, M.D.
Department of Radiology, The Affiliated Hospital of Qingdao University
Postal address: No.59 Haier Road, Qingdao, China, 266000
E-mail: zhiminglee@yeah.net
TEL: +86 0532-82913099

Abstract

BACKGROUND: Acute liver injury (ALI) is characterized by excessive reactive oxygen species (ROS) accumulation and severe inflammation, lacking effective imaging-guided targeted therapy.

PURPOSE or HYPOTHESIS: This study fabricated L-arginine-modified manganese-doped mesoporous polydopamine nanoparticles (AMM NPs) and explored their dual functions of MRI visualization and ROS-scavenging/anti-inflammatory treatment for ALI.

POPULATION or SUBJECTS: AML12 hepatocytes and thioacetamide-induced ALI rat models were used. Mn-MPDA NPs (MM NPs) were prepared as the control.

ASSESSMENT: The physicochemical properties, cytotoxicity, cellular uptake, and ROS elimination ability of AMM NPs were evaluated. In vivo MRI monitoring, hepatic pathological staining, ROS levels, and serum ALT, AST, TNF-α, and IL-6 were detected to assess imaging performance and therapeutic efficacy.

RESULTS: AMM NPs exhibited uniform spherical morphology, favorable particle size, stable zeta potential, and satisfactory L-Arg loading capacity and longitudinal relaxivity. AMM NPs showed high biosafety and time-dependent cellular uptake. The intracellular ROS level was significantly reduced by 33.64% in the AMM group ($p < 0.001$). In ALI models, AMM NPs prominently increased hepatic ΔT1 values for injured liver visualization. After treatment, the inflammatory area, hepatic ROS level, and serum ALT, AST, TNF-α, and IL-6 levels were markedly improved compared with the ALI group (all $p < 0.05$).

DATA CONCLUSION: The synthesized AMM NPs possess excellent biocompatibility, accurate T1-weighted MRI imaging capability, and robust ROS scavenging and anti-inflammatory effects. This nanoparticle provides a promising imaging theranostic strategy for precise diagnosis and treatment of acute liver injury.

Keywords: Acute liver injury; Magnetic resonance imaging; Nanoparticles; Oxidative stress

Introduction

Acute liver injury (ALI) is a severe and life-threatening clinical syndrome triggered by multiple pathogenic factors including viral infection, hepatotoxic drugs, alcohol abuse, and hypoxia. Pathologically, ALI is characterized by widespread hepatocellular necrosis within a short time frame, along with robust inflammatory infiltration and coagulation disorders. Patients with ALI usually present an unfavorable clinical prognosis(1, 2).

During the intricate pathological process of ALI, oxidative stress and overaccumulation of ROS have been universally acknowledged to serve as the pivotal mechanism underlying hepatocyte injury(3).When liver tissue is exposed to pathogenic factors such as drugs or toxins, mitochondrial dysfunction is induced in hepatocytes. This leads to excessive intracellular reactive oxygen species (ROS) production that exceeds the scavenging capacity of the endogenous antioxidant system, including superoxide dismutase (SOD) and glutathione peroxidase (GSH-Px), thereby disrupting intracellular redox homeostasis(4).Excessively generated ROS act as potent signaling molecules, inducing hepatocytes to secrete a variety of inflammatory mediators. These mediators further recruit and activate immune cells such as neutrophils and macrophages, thereby initiating and amplifying the local inflammatory cascade response (5).Targeted scavenging of excessive ROS in the liver to restore disrupted redox homeostasis is regarded as a viable strategy to remodel the local hepatic microenvironment, halt disease pathogenesis, and alleviate overall pathological progression(6, 7).

Although the understanding of the pathological mechanisms underlying acute liver injury (ALI) has been continuously deepened, and the central role of oxidative stress has become increasingly clear, the diagnosis and therapeutic targeting of oxidative stress still face substantial clinical challenges. Although serological biomarkers, including alanine aminotransferase (ALT) and aspartate aminotransferase (AST), can reflect the degree of hepatocellular injury, they lack sufficient specificity(8).Moreover,

systemically administered antioxidants (e.g., N-acetylcysteine) suffer from pharmacokinetic limitations, such as poor liver targeting ability and insufficient local drug concentration at the lesion site(9).

Notably, the advancement of nanotechnology offers a novel avenue for the diagnosis and treatment of liver diseases, among which magnetic resonance imaging (MRI) has been widely applied in clinical practice due to its excellent soft tissue resolution and non-invasive characteristics. Gadolinium-based contrast agents have been widely used as paramagnetic contrast agents, yet their safety concerns have attracted increasing attention, including potential risks such as the induction of nephrogenic systemic fibrosis and gadolinium deposition(10).Nevertheless, manganese (Mn)-based MRI contrast agents provide a promising alternative to conventional gadolinium-based contrast agents due to their superior relaxivity and favorable biosafety profile(11).In terms of carrier selection, mesoporous polydopamine (MPDA) serves as an ideal platform for nanocarriers owing to its excellent biocompatibility, abundant surface functional groups, and unique physicochemical properties. Moreover, MPDA itself has also been reported to possess the capability of scavenging ROS. Scavenging excessive ROS is mainly attributed to the high specific surface area endowed by MPDA's mesoporous structure, which exposes more active sites and thereby eliminates ROS more efficiently(12, 13).L-arginine (L-Arg), a conditionally essential amino acid, exhibits multiple biological regulatory effects including anti-inflammatory, antioxidant and anti-apoptotic activities. It can synergize with the ROS-scavenging property of MPDA to ameliorate the inflammatory microenvironment at the injured site(14).Therefore, the introduction of L-Arg can enhance the nanosystem with additional therapeutic efficacy. After intravenous injection, the in vivo distribution of nanoparticles (NPs) is closely related to their physicochemical properties, including particle size, surface charge, and hydrophilicity and hydrophobicity. NPs within a certain size range can be actively internalized by Kupffer cells (KCs) in the hepatic sinusoids, or passively accumulate at pathological sites with increased vascular permeability (e.g., inflammatory lesions) via the enhanced permeability and retention (EPR) effect(15).These two mechanisms collectively facilitate the relative

accumulation of nanoparticles in the liver, and provide a theoretical basis for the targeted delivery of diagnostic and therapeutic functions to hepatic tissues(16).

In this study, we aimed to construct a type of theranostic nanoparticle (Arg-Mn-MPDA nanopariticles, AMM NPs) based on L-Arg, Mn, and MPDA for the diagnosis and treatment of acute liver injury. For AMM NPs, the high relaxivity of Mn^{2+} with T1 mapping sequences could enable quantitative assessment of damaged liver tissue, while the ROS-scavenging MPDA core and surface-functionalized L-Arg could synergistically mitigate oxidative stress and resolve the inflammatory microenvironment in injured liver. Our study provided a novel nanotheranostic strategy with great translational potential for the early diagnosis and treatment of ALI.

Material and methods

The animal study protocol was approved by our institutional ethics committee (Approved No.: QYFY WZLL 42335). All animal experimental procedures were strictly conducted in compliance with relevant laboratory guidelines and adhered to the 3R ethical principles of Replacement, Reduction, and Refinement. Specifically, alternative non-animal approaches were utilized wherever feasible. The number of experimental animals was kept to a minimum, and experimental protocols were optimized to minimize animal distress and discomfort.

Reagents and consumables

1,3,5-Trimethylbenzene (TMB), absolute ethanol and acetone were purchased from Sinopharm Chemical Reagent Co., Ltd. Dopamine hydrochloride (DA·HCl), manganese chloride tetrahydrate ($MnCl_2·4H_2O$), and L-Arg were purchased from Shanghai Aladdin Biochemical Technology Co., Ltd.Pluronic® F-127 was purchased from Merck Group, Darmstadt, Germany. Tris(hydroxymethyl)aminomethane (Tris), Nile Red, and Reactive Oxygen Species Assay Kit (DCFH-DA) were purchased from Beijing Solarbio Science & Technology Co., Ltd. Fetal bovine serum (FBS) was purchased from Sichuan NuohongHuikang Biotechnology Co., Ltd. Trypsin Cell Digestion Solution (with phenol red) was purchased from Beijing Labgic Technology Co., Ltd. SuperKine™ High-Sensitivity Cell Proliferation Assay Kit (CCK-8) and

Rapid Cell Cryopreservation Medium (Serum-free, Protein-free) were purchased from Aiboxin (Wuhan) Biotechnology Co., Ltd. Immunostaining Permeabilization Solution (Triton X-100) was purchased from Beyotime Biotechnology Co., Ltd., Shanghai. Lipopolysaccharides (LPS) were purchased from Shanghai Haoyuan Biomedical Technology Co., Ltd.DMEM high-glucose medium (containing double antibiotics), phosphate buffered saline (PBS), and cytoskeleton green fluorescent probe were purchased from Jiangsu KeyGen Biotech Co., Ltd. Anti-fade Mounting Medium (containing DAPI) was purchased from Dalian Meilun Biotechnology Co., Ltd. Tumor necrosis factor-α (TNF-α) and interleukin-6 (IL-6) ELISA kits were purchased from Shanghai Youxuan Biotechnology Co., Ltd. All experimental reagents used were of analytical grade. All water used in the experiments was ultrapure water.

Synthesis and preparation of AMM NPs

The synthesis and preparation of AMM NPs in this study referred to the established protocol reported in the literature(17), with appropriate modifications. AMM NPs were synthesized according to the following procedures. First of all, 200 mg of Pluronic® F-127 and 200 mg of TMB were dissolved in a mixed solution containing 25 mL of ultrapure water and 25 mL of ethanol, followed by stirring for 30 minutes. Meanwhile, 30 mg of L-Arg was dissolved in 10 mL of Tris solution at pH 8, which was then added to the above mixed solution and stirred for another 30 minutes. Subsequently, 60 mg of DA·HCl and 2 mg of $MnCl_2 \cdot 4H_2O$ were dissolved in 3 mL of ultrapure water. After stirring for 24 hours, the mixture was introduced into the foregoing solution and continuously stirred for another 24 hours. The resulting solution was centrifuged at 13000 r/min for 15 minutes. Afterwards, the obtained precipitate was washed with a mixed solution of 20 mL ethanol and 10 mL acetone and centrifuged three times. Finally, the product was lyophilized for 24 hours to obtain black Arg-Mn-MPDA (AMM) NPs powder for subsequent use. In addition, 10 mL of Tris solution (pH 8) was used to replace the L-Arg solution to prepare Mn-MPDA (MM) NPs as the control group.

Characterization of AMM NPs

Transmission electron microscope (TEM) An amount of 0.1 mg/mL ethanol solutions of MM NPs and AMM NPs were separately pipetted and dropped onto

dedicated copper grids to allow uniform spreading of the solution. The copper grids were placed at room temperature for natural drying. After complete volatilization of the solvent, the samples were observed by TEM.

Determination of NPssize and zeta potential An aliquot of 1–2 mL MM NPs and AMM NPs solutions with a concentration of 0.1 mg/mL were separately transferred into cuvettes, ensuring no air bubbles remained on the liquid surface. The cuvettes were placed into a Malvern nanoparticle size and zeta potential analyzer to determine the NPs size and zeta potential of the samples.

Specific surface area and pore size analysis80–100 mg of MM NPs powder was accurately weighed, and its specific surface area and pore size were determined via a fully automated specific surface area and porosity analyzer. Before measurement, the sample was degassed under vacuum at 120 °C for 10 hours to eliminate volatile impurities. With high-purity nitrogen serving as the adsorbate, nitrogen adsorption-desorption isotherms were acquired at −196 °C, and the specific surface area together with pore size distribution was subsequently calculated.

Thermogravimetric analysis (TGA)5–10 mg of MM NPs and AMM NPs samples were accurately weighed, which were tested using a thermogravimetric analyzer under a nitrogen atmosphere. The temperature was increased from 50 °C to 600 °C at a heating rate of 10 °C/min. The loading rate of L-Arg in AMM NPs was calculated according to the difference in weight loss ratio between MM NPs and AMM NPs.

Determination of T1 relaxivity The in vitro T1 relaxivity of AMM was determined using a 3.0 T magnetic resonance imaging scanner (Magnetom Skyra, Siemens Medical Solutions, Erlangen, Germany).The detailed procedures were as follows: AMM NPs powder was dispersed in ultrapure water to prepare a series of aqueous solutions with mass concentrations of 0, 0.005, 0.0125, 0.025, 0.05 and 0.1 mg/mL, respectively. All samples with different concentrations were scanned at room temperature using a T1 mapping sequence. The corresponding T1 relaxation time of each sample was acquired via the post-processing software (Syngo.VIA). Linear fitting was performed with mass concentration (mg/mL) as the abscissa and longitudinal relaxation rate (R_1=1/T1, s^{-1}) as the ordinate. The slope of the fitted straight line was defined as the longitudinal

relaxivity (r_1) of the material.

In vitro cell experiments

Cytotoxicity assay

AML12 cells were resuspended in 15 mL centrifuge tubes to generate a homogeneous single-cell suspension. Cell concentration was quantified using a hemocytometer under an optical microscope, and the cell density was subsequently adjusted to 5×10^4 cells/mL with complete growth medium. The cell suspension was then seeded into 96-well culture plates at a volume of 0.1 mL per well, with a final density of 5×10^3 cells per well. The plated cells were incubated at 37 °C in a humidified incubator containing 5% CO_2 for 24 hours to allow sufficient cell adhesion prior to subsequent drug intervention.

After 24 hours of adherent culture, the original medium in each well was discarded and replaced with fresh complete medium containing different concentrations of AMM NPs. The final concentration gradients of AMM NPs were set at 50, 100, 150, 200, 250 and 300 μg/mL, with three replicate wells for each concentration. The culture plate was returned to the incubator for another 24 hours of incubation to observe the effects of different AMM doses on cell viability.

To accurately evaluate cell viability, four parallel control groups were established simultaneously in this experiment: Group G1: Cells, complete medium, CCK-8 solution and AMM solution were included; Group G2: Cells, complete medium and CCK-8 solution were included; Group G3: Complete medium, CCK-8 solution and AMM solution were included; Group G4: Only complete medium and CCK-8 solution were included.

After the completion of drug intervention, 10 μL of CCK-8 solution was added to each well in the dark. The plate was gently shaken to ensure thorough mixing of the CCK-8 reagent with the culture medium. Subsequently, the plate was incubated for another 2 hours in the incubator, with any movement avoided throughout the incubation period to guarantee consistent reaction conditions. Upon incubation termination, the absorbance (A) of each well was detected at 450 nm using a microplate reader.

Cell viability was calculated according to the following formula:

$$\text{Cell viability (\%)} = [(A1 - A3)/(A2 - A4)] \times 100\%$$

Where, A1, A2, A3 and A4 refer to the absorbance in Group A1, Group A2, Group A3, and Group A4, respectively.

Intracellular ROS scavenging

AML12 cells were seeded in six-well plates. An oxidative stress injury model was constructed by LPS stimulation, and the intracellular ROS level was determined using the ROS-sensitive fluorescent probe DCFH-DA.

The cells were divided into five experimental groups: control, LPS, LPS + L-Arg, LPS + MM NPs, and LPS + AMM NPs. Except for the control group, all other groups were first stimulated with 1 μg/mL LPS for 24 hours. Subsequently, the culture medium was replaced with fresh complete medium supplemented with L-Arg, MM NPs, or AMM NPs, and the cells were incubated for an additional 4 hours. The concentration of L-Arg and MM NPs was normalized to the corresponding constituent content in 300 μg/mL AMM NPs according to the loading rate, and the final concentration of AMM NPs was set at 300 μg/mL.After treatment, the culture medium of each group was discarded, and the cells were washed three times with serum-free medium. Subsequently, 1 mL of DCFH-DA working solution was added to each well. The working solution was freshly prepared by diluting the DCFH-DA DMSO stock solution with serum-free medium to a final concentration of 8 μM, with the final DMSO concentration maintained below 0.1%. The cells were then incubated at 37 °C and 5% CO_2 for 30 min in the dark. After incubation, the cells were immediately washed thoroughly three times with PBS to remove residual DCFH-DA probe. Subsequently, green fluorescence images reflecting intracellular ROS production were observed and captured under a fluorescence microscope. Fluorescence intensity was quantitatively analyzed using Image J software (Version 1.53).

Cellular uptake assay

AML12 cells were seeded into confocal laser scanning microscopy dishes with glass bottoms at a density of 1×10^5 cells per dish and pre-cultured for 24 hours to allow full adhesion and reach an optimal experimental state. At the start of the experiment, the original medium was discarded and replaced with fresh complete medium containing

Nile Red-labeled AMM NPs at a final concentration of 200 μg/mL. To investigate the cellular uptake of AMM NPs, the cells were incubated in an incubator at different time points of 0.5, 1, 1.5, 2, and 4 hours, respectively.

Upon reaching each predetermined time point, the culture medium was aspirated away, and the cells were rinsed three times with PBS to remove unbound Nile Red-labeled AMM NPs. Subsequently, 4% paraformaldehyde solution was added to fix the cells at room temperature for 15 minutes. After fixation, the cells were washed with PBS and permeabilized with 0.1% Triton X-100 at room temperature for 10 minutes to increase cell membrane permeability. Following permeabilization, the cells were rinsed three times with PBS.

Fluorescent staining was performed sequentially. Firstly, the cytoskeleton was stained with FITC-conjugated phalloidin (1:1000) and incubated at room temperature for 40 min in the dark, followed by three PBS washes to remove excess dye. Thereafter, 300 μL of DAPI-containing antifade mounting medium was added to stain the cell nuclei, and the samples were incubated at room temperature for 15 min under light-protected conditions, then rinsed three times with PBS again. Fluorescence images were acquired using a high-resolution confocal laser scanning microscope. For quantitative analysis, Image J software (Version 1.53) was applied to statistically analyze the red fluorescence intensity at each time point, and the cellular uptake level was presented as the mean fluorescence intensity.

In vivo animal experiments

Experimental animal selection and feeding conditions

Male Wistar rats aged 8 weeks with a body weight ranging from 230 to 300 g were utilized in the present study. All experimental animals were purchased from Shandong Pengyue Laboratory Animal Technology Co., Ltd. All rats were housed in a specific pathogen-free (SPF) animal room. The housing environment was maintained at a constant temperature of 20–23 °C with a relative humidity of 50%–80%, and a 12- hour light/dark cycle was applied. All animals were acclimatized for one week prior to the experiment, with free access to standard laboratory chow and drinking water throughout the acclimation period. The entire feeding procedure was conducted in strict accordance

with SPF-grade management standards, including regular replacement of cages and bedding, provision of fresh and sterile food and water, as well as routine disinfection of the rearing environment.

In vivo biotoxicity evaluation of AMM NPs

Six healthy male Wistar rats were randomly divided into two groups: the experimental group and the control group, with three rats in each group. Rats in the experimental group were injected intravenously via the tail vein with AMM NPs dissolved in normal saline at a concentration of 2 mg/mL and a dosage of 3 mL/kg body weight. The control group received an equal volume of normal saline via tail vein injection.

Twenty-four hours after administration, the rats were deeply anesthetized with isoflurane and sacrificed, followed by body weight measurement. The major parenchymal organs, including the heart, liver, spleen, lungs, and kidneys, as well as whole blood samples, were immediately collected. Samples of these organs were fixed in 10% neutral buffered formalin, embedded in paraffin, and subsequently stained with hematoxylin and eosin (H&E). Histopathological alterations and tissue necrosis were observed under an optical microscope. After the whole blood samples were centrifuged to separate serum, the serum levels of ALT and AST were detected using a fully automatic biochemical analyzer to evaluate the degree of liver function injury.

Establishment of an acute liver injury rat model

A thioacetamide (TAA)-induced rat model of acute liver injury (ALI) was adopted in our study. A total of 10 male Wistar rats were enrolled and randomly assigned into the ALI group and the control group, with 5 rats in each group. In the ALI group, the acute liver injury model was established via a single intraperitoneal injection of TAA saline solution at a dose of 500 mg/kg. The control group was given an equal volume of normal saline by intraperitoneal injection. The general physiological status of the animals was closely monitored after injection. At 24 hours after TAA administration, rats in both groups were injected with AMM NPs solution through the tail vein, followed by MRI scanning to evaluate the in vivo distribution and imaging performance of AMM NPs.

In vivo MR imaging

All MR scans in our study were performed on a 3.0 T MRI system (Magnetom Skyra, Siemens Medical Solutions, Erlangen, Germany), with an 8-channel phased-array dedicated small-animal coil (Shanghai Chenguang Medical Technology Co., Ltd.). During scanning, the ambient temperature was maintained at a constant 25 °C, and the animals were fixed in a head-first prone position. The key imaging parameters for the T1 mapping sequence were set as follows: echo time (TE) of 2.19 ms, repetition time (TR) of 5.48 ms, field of view (FOV) of 80 mm × 60 mm, slice thickness of 2 mm, and four signal averages (NSA). All experimental animals, including both healthy control rats and TAA-induced ALI model rats, were subjected to isoflurane inhalation anesthesia. Image acquisition was initiated once a stable deep anesthetic plane was achieved.

The imaging procedure was performed as follows: First, baseline MR images were acquired before AMM NPs administration. Subsequently, AMM NPs saline solution was injected via the tail vein. Repeated MR image acquisitions were then conducted at four time points of 0.5, 1, 1.5, and 2 hours after AMM NPs administration.

After image acquisition, the MR data were imported into a workstation for post-processing and analysis. On the maximal axial slice of the liver at each time point, three regions of interest (ROIs) with a fixed area of approximately0.5 cm^2 were manually delineated on T1 mapping. During ROI placement, blood vessels, bile ducts, and macroscopically visible lesion areas were carefully avoided. The arithmetic mean of the measured values from the three ROIs was calculated. The differences in T1 relaxation time (ΔT1) between post-administration and baseline pre-administration at each time point were computed for subsequent statistical analysis.

Evaluation of therapeutic efficacy

Fifteen healthy male Wistar rats were randomly divided into the control group, ALI group and treatment group, with five rats in each group. Rats in both the ALI group and the treatment group were established with ALI model via a single intraperitoneal injection of thioacetamide (TAA) saline solution, and rats in the control group received an equal volume of normal saline by intraperitoneal injection. Twenty-four hours after ALI model establishment, rats in the treatment group were injected with AMM NPS

solution via the tail vein, with a frequency of once a day for two consecutive days. Rats in the control group and ALI group were administered an equal volume of normal saline in the same manner and dosage. Twenty-four hours after the last administration, the rats were deeply anesthetized via isoflurane inhalation. Fresh liver tissues and whole blood samples from the abdominal aorta were promptly collected via laparotomy. Liver tissue samples were collected and fixed in 10% neutral buffered formalin. Subsequently, the specimens were embedded in paraffin and sliced into sections, followed by hematoxylin and eosin (H&E) staining. The pathological morphological alterations and necrotic severity of hepatic tissues were observed under a light microscope. Fresh liver tissue samples were additionally collected for the detection of ROS levels. After the collected blood samples were centrifuged to isolate serum, the serum levels of ALT, AST, TNF-α and IL-6 were determined to evaluate the degree of liver injury and inflammatory response.

Statistical analysis

All statistical analyses were performed using SPSS version 27.0. Continuous variables were expressed as mean±standard deviation. An independent sample *t*-test or analysis of variance was used to determine the statistical significance between groups, and the p value less than 0.05 was considered statistically significant.

Results

Characterization of AMM NPs and MM NPs

A series of morphological and structural characterizations were performed on AMM NPs and MM NPs samples. TEM showed that both AMM NPs and MM NPs exhibited uniformly distributed spherical morphology, with particle sizes of 100.65±9.12 nm and 129.75±2.19 nm, respectively (Figure 1A, B).Nitrogen adsorption-desorption measurements were further performed to analyze the porous structure. The isotherm of MM NPs exhibited a typical Type IV feature with a distinct hysteresis loop, confirming that the material is predominantly mesoporous. The pore size distribution curve further supported the characteristics of mesoporous(Figure 1C, D).

A Malvern nanoparticle size and zeta potential analyzer was used to measure the

hydrodynamic diameters of nanoparticles in solution (Figure 1E). The results showed that the hydrodynamic diameters of AMM NPs and MM NPs were189.87±2.24 nm and 170.67±2.53 nm, respectively, which deviated from the TEM results. This deviation was mainly attributed to the increased apparent size caused by the hydration layer on the particle surface during measurement(18). Notably, the particle size of AMM NPs was still larger than that of MM NPs, which was consistent with the trend reflected by TEM. The surface electrical properties were characterized by zeta potential (Figure 1F). The zeta potential of MM NPs was approximately −38.10±0.44 mV, while that of L-Arg-modified AMM NPs changed to −34.50±0.36 mV. The combined changes in particle size and surface potential indicated that L-Arg was successfully modified onto the surface of nanoparticles. Therefore, AMM NPs were successfully constructed.

TGA analysis on AMM NPs and MM NPs was shown in Figure 1G.When the temperature rose to 600 °C, the residual mass fraction of MM NPs was 53.53% (cumulative weight loss rate of 46.47%), while the residual mass fraction of AMM NPs was 49.51% (cumulative weight loss rate of 50.49%).The cumulative weight loss rate of AMM NPs was higher than that of MM NPs, which was mainly attributed to the thermal decomposition of L-Arg modified on the AMM NPs surface. Accordingly, the loading content of L-Arg in AMM NPs was calculated to be approximately 4.02%. At room temperature, a 3.0T MR scanner was used to measure the T_1 relaxation times of AMM NPs at different mass concentrations（Figure 2A）. By fitting the linear relationship between the longitudinal relaxation rate ($1/T_1$) and nanoparticle concentration (Figure 2B), the longitudinal relaxivity (r_1) of the material was calculated to be 5.7 mL/(mg·s). This relaxivity value reflects the ability of the nanoparticles to shorten the T_1 relaxation time of water protons per unit concentration. The shortening effect of T_1 relaxation time was attributed to the efficient loading and rigid immobilization of Mn^{2+} by the mesoporous polydopamine structure. The formed hydrophilic and porous environment greatly facilitated the effective exchange between water molecules and paramagnetic manganese centers. The above results confirmed the great potential of AMM NPs as an efficient T_1 contrast agent.

In vitro cell experiments

AML 12 cells were co-incubated with AMM NPs at different concentrations (50–300 μg/mL) for 24 h, and the cell viability remained at a relatively high level (Figure 3). Even at the highest concentration (300 μg/mL), the cell viability was still higher than 90%. These results indicated that AMM NPs exhibited no obvious cytotoxicity and possessed favorable in vitro biosafety.

Fluorescence microscopy observations revealed that the intracellular green fluorescence intensity was markedly elevated in the LPS group relative to the normal control group, indicating extensive intracellular ROS accumulation. Following intervention with different formulations, the fluorescence intensity in each treatment group declined to varying extents. Notably, the LPS + AMM group displayed the most pronounced attenuation of fluorescence signals (Figure 4).Quantitative analysis of fluorescence intensity revealed that the average fluorescence intensity in the LPS group increased by approximately 61.01% compared with the control group ($p< 0.001$) (Figure 5), and it was confirmed that LPS successfully induced cellular oxidative stress. Compared with the LPS group, the fluorescence intensities of the LPS + L-Arg, LPS + MM, and LPS + AMM groups were all decreased. Among them, the AMM-treated group exhibited the most remarkable reduction in fluorescence intensity by approximately 33.64% ($p< 0.001$) relative to the LPS group. Thus, it is demonstrated that AMM NPs could effectively eliminate LPS-induced excessive ROS.

Fluorescence images revealed that the cellular uptake of AMM NPs (red fluorescence) exhibited an obvious time-dependent manner. After 0.5 hour of co-incubation, weak red fluorescence signals were observed in the cytoplasmic region, and that indicated the rapid internalization of AMM NPs by cells. Intracellular fluorescence intensity increased markedly as the co-incubation time prolonged. Quantitative analysis using Image J demonstrated that the average fluorescence intensity reached its peak at 1 hour, which was markedly higher than that at all other time points ($p< 0.001$).As the incubation time was further prolonged to 2 and 4 hours, intracellular fluorescence intensity exhibited a gradual decline. These results indicated that AMM nanoparticles could be efficiently internalized by AML12 cells, with the uptake efficiency reaching the maximum at approximately 1 hour.

In vivo animal experiments

In vivo biotoxicity evaluation

All animals survived throughout the entire experimental observation period. When compared with the control group, no obvious abnormalities were observed in the general conditions of rats in the experimental groups, including behavioral performance, spontaneous activity, food and water intake, and hair appearance. There was no statistically significant difference in the final body weight of rats between the experimental group and the control group (Figure 6; experimental group, 267.50±7.37 g; control group, 275.20±9.09 g; $p > 0.05$).The major visceral organs including the heart, liver, spleen, lung and kidney of rats in the experimental groups presented fresh color, regular morphology and normal size. No macroscopically visible bleeding spots, abnormal swelling, atrophy or discoloration were observed in any of these organs. Morphological observation via H&E-stained sections showed that the tissue structure of the experimental group remained intact, with no specific pathological lesions detected(Figure 7).

Evaluation of the Acute Liver Injury Model in Rats

For the ALI rat model, histopathological results revealed that rats in the ALI group exhibited typical acute injury lesions in liver tissues, characterized by diffuse hepatocellular edema and vacuolar degeneration. Scattered focal or patchy necrotic areas were observed, accompanied by inflammatory cell infiltration predominantly composed of neutrophils and lymphocytes (Figure 8).The serum levels of ALT and AST activities in the ALI group were markedly elevated compared with the control group (ALI group vs control group: ALT, 844.6±153.6 U/L vs 40.2±5.5 U/L; AST, 4911.0±554.0 U/L vs 110.2±6.3 U/L;$p < 0.001$).

In Vivo MRI

The MRI scanning results clearly revealed the differences among all experimental groups as well as their dynamic changes over time (Figure 9). Before AMM NPs injection, T_1 mapping images of the liver in the normal control rats displayed typical homogeneous signal characteristics corresponding to healthy liver tissue, whereas T_1 mapping images of rats in the ALI group exhibited inhomogeneous liver signals. After

AMM NPs injection in the ALI group, the liver T_1 values on T_1 mapping images at all time points were lower than those before injection. The T_1 values decreased to the lowest point at 1-hour post-administration, and then gradually recovered over time. In the normal control group, a similar declining trend of hepatic T_1 values was also detected following AMM injection, with the T_1 values dropping to the minimum at 1-hour post-injection and then gradually recovering thereafter. The liver ΔT_1 values in both the ALI and control groups reached their maximum at 1 hour, followed by a gradual decrease thereafter. Furthermore, the ΔT_1 value in the ALI group was higher than that in control group (358.7±46.5 vs 162.0±15.9, $p< 0.001$).

Evaluation of Therapeutic Efficacy

Histopathological examination revealed that the normal control group displayed intact hepatic lobular architecture with regularly arranged hepatic cords and morphologically normal hepatocytes; no hepatocellular edema, degeneration or inflammatory cell infiltration was observed. In the ALI group, prominent morphological manifestations of acute liver injury were evident, including disrupted hepatic lobular structure, diffuse hepatocellular edema with severe vacuolar degeneration, and patchy inflammatory infiltration dominated by neutrophils and lymphocytes. In the AMM NPs treatment group, although mild liver injury features remained, both the severity and extent of pathological lesions were notably ameliorated relative to the ALI group. Hepatocellular edema and vacuolation were substantially attenuated, accompanied by a marked reduction in the scope of inflammatory cell infiltration (Figure 10). Semiquantitative analysis of H&E-stained sections showed that the percentage of inflammatory area in hepatic tissue sections was significantly reduced in the AMM NPs treatment group relative to the ALI group (24.8±2.3% vs 15.4±1.4%, $p< 0.001$) (Figure 11A).

At the molecular mechanism level, the ROS levels detected in liver tissues paralleled the histological changes (Figure 11B).Compared with the normal control group, the level of reactive oxygen species (ROS) in the liver was markedly increased in the ALI group (667.7±59.5 vs 1338.1±168.3, $p< 0.001$).Following AMM NPs intervention, hepatic ROS levels in the AMM NPs treatment group were significantly lower than

those in the ALI group with no AMM NPs treatment (1095.9±97.5 vs 1338.1±168.3, $p< 0.05$).

Inflammatory cytokine detection results revealed that compared with the normal control group, the hepatic levels of TNF-α and IL-6 were significantly elevated in the ALI group (TNF-α: 127.2±11.4 pg/mL vs 292.7±32.8 pg/mL; IL-6: 24.9±2.1 pg/mL vs 76.1±10.6 pg/mL, $p< 0.001$) (Figure 11C).Upon AMM NPs intervention, hepatic TNF-α and IL-6 concentrations were markedly downregulated when compared with the ALI group (TNF-α: 199.2±22.4 pg/mL vs 292.7±32.8 pg/mL; IL-6: 43.4±8.5 pg/mL vs 76.1±10.6 pg/mL, $p< 0.05$).Serum ALT and AST increased dramatically in the ALI group and were markedly higher than in the normal control group (ALT: 37.8±4.9 U/L; AST: 118.2±8.4 U/L vs 830.6±168.6 U/L and 5081.0±462.5 U/L, respectively; $p< 0.001$) (Figure 11D).Serum ALT and AST activities were markedly decreased in the AMM-treated group compared with the ALI group (ALT: 321.4±35.1 U/L vs 830.6±168.6 U/L; AST: 1690.6±237.7 U/L vs 5081.0±462.5 U/L, $p< 0.01$).

Discussion

In our study, we successfully constructed and verified that AMM NPs could be applied to the diagnosis and treatment of ALI. In vitro and in vivo experiments showed that AMM NPs had satisfactory biosafety and could effectively scavenge ROS. And H&E staining and serum biochemical assays further verified that AMM could alleviate hepatic oxidative stress and suppress inflammation. Quantitative T1 mapping analysis revealed that AMM NPs with ΔT_1 value could allows for the reliable discrimination between acute liver injury and normal liver parenchyma.

Although traditional broad-spectrum antioxidants such as N-acetylcysteine have shown certain efficacy in the prevention and treatment of ALI, their rapid in vivo clearance, insufficient targeted accumulation at lesion sites and resultant low bioavailability severely restrict their clinical translation and practical application(19, 20). To realize the MR imaging and therapeutic effects of AMM NPs in ALI, their enrichment in injured liver tissue should be confirmed. In our study, T_1 mapping technology with AMM NPs was used to quantitatively detect changes in hepatic T_1

values in ALI animal models. The difference of T_1 value before and after enhancement (ΔT_1) was adopted as a quantitative index to reflect the enrichment level of AMM NPs in the liver. Our results showed that injection of AMM NPs via tail vein, the T1 values in both the normal and ALI groups decreased initially and then gradually recovered, and achieved the minimum at 1 hour post-injection. This trend was consistent with the cellular uptake results, in which the intracellular fluorescence intensity of AMM NPs peaked at 1 hour. Despite the similar variation tendency, the ΔT_1 of the ALI group was significantly higher than that of the normal group at 1 hour after injection. These findings indicate that AMM NPs can accumulate in acute injured livers. The enrichment of AMM NPs in the liver with acute liver injury may be attributed to the mechanisms including inflammation-induced increased vascular permeability, enhanced phagocytic activity of Kupffer cells and altered cell membrane integrity.

The therapeutic efficacy of AMM NPs against acute liver injury was systematically validated from four aspects in our study: histopathological changes, oxidative stress, inflammatory response and liver function. Compared with the untreated ALI group, the AMM treatment group showed markedly alleviated hepatocellular edema and vacuolation, accompanied by a significant reduction in the scope of inflammatory cell infiltration. In the LPS-induced cellular oxidative stress model, AMM NPs intervention markedly and significantly reduced intracellular ROS levels compared with the LPS group. This effect was further validated in subsequent in vivo experiments. Detection of ROS levels in liver tissue demonstrated that AMM intervention effectively reduced hepatic ROS accumulation and alleviated the oxidative stress state in the ALI model. Serological results revealed that AMM markedly reduced the levels of pro-inflammatory cytokines TNF-α, IL-6, as well as serum ALT and AST. The core mechanism underlying the therapeutic efficacy of AMM NPs may lie in two aspects including efficient ROS scavenging and regulation of the inflammatory microenvironment. The MPDA carrier possesses a high specific surface area to provide abundant active sites and expose more reactive catechol groups, which effectively eliminate excess free radicals and relieve oxidative stress(21). Meanwhile, L-Arg, as an NO precursor, indirectly modulates oxidative stress(22). L-Arg can also upregulate the

transcription of antioxidant-related genes and promote Nrf2 protein synthesis by activating the Akt-Nrf2 signaling pathway(23). The combination of the above two effects specifically interferes with the vicious cycle of "oxidative stress-inflammation" in ALI, ultimately ameliorating the pathological progression of acute liver injury.

Our study has some limitations. First, in terms of the in vivo therapeutic evaluation, this study mainly focused on the AMM NPs treatment group. Although in vitro cell experiments preliminarily showed that AMM NPs had superior ROS scavenging capacity. However, the complexity of the in vivo microenvironment makes it difficult to strictly clarify whether the therapeutic advantages of AMM NPs originate from the antioxidant activity of the MPDA carrier, the anti-inflammatory synergism introduced by L-Arg modification, or the combined contribution of both. Further in vivo groups containing only MM and L-Arg should be established in future work to systematically dissect the functional contribution of each component of AMM. Second, AMM NPs accumulates in the liver mainly through size-based passive targeting, and its targeting efficacy and specificity are in need of further improvement. Third, the long-term in vivo metabolic pathway and biosafety profile of AMM NPs remain to be elucidated. Further systematic long-term toxicity studies are therefore needed for its comprehensive safety evaluation. Finally, given that only the TAA-induced ALI model was employed in this study, the applicability and generalizability of the current findings to ALI triggered by other etiologies including drug-induced, viral, and ischemia-reperfusion injury, requires further validation using diverse experimental models.

In conclusion, AMM NPs can passively target and accumulate in acute liver injury lesions, and exert prominent ROS scavenging and anti-inflammatory bioactivities. Meanwhile, its favorable T1-shortening effect endows it with MRI imaging capability. Accordingly, AMM NPs emerge a promising integrated theranostic strategy for acute liver injury.

Acknowledgments

Thanks to Dr. Li for his guidance and support in this study

Reference

1. Z. Gao *et al.*, Hydroxytyrosol Alleviates Acute Liver Injury by Inhibiting the TNF-α/PI3K/AKT Signaling Pathway via Targeting TNF-α Signaling. *Int J Mol Sci* **25** (2024).
2. Y. Yang *et al.*, Visualization of therapeutic intervention for acute liver injury using low-intensity pulsed ultrasound-responsive phase variant nanoparticles. *Biomater Sci* **12**, 1281-1293 (2024).
3. X. Yuan *et al.*, Preventing acute liver injury via hepatocyte-targeting nano-antioxidants. *Cell Prolif* **56**, e13494 (2023).
4. A. Allameh, R. Niayesh-Mehr, A. Aliarab, G. Sebastiani, K. Pantopoulos, Oxidative Stress in Liver Pathophysiology and Disease. *Antioxidants (Basel)* **12** (2023).
5. T. Qin *et al.*, NIR Driven Pd/Cerium Oxide Nano-Heterojunction for Enhanced Salvaging Sepsis Induced Acute Liver Injury via Reprogramming Redox Homeostasis in Synergy with Inducing Autophagy. *Adv Sci (Weinh)* **12**, e17252 (2025).
6. X. Wu *et al.*, Scavenging ROS to Alleviate Acute Liver Injury by ZnO-NiO@COOH. *Adv Sci (Weinh)* **9**, e2103982 (2022).
7. D. Ni *et al.*, Ceria Nanoparticles Meet Hepatic Ischemia-Reperfusion Injury: The Perfect Imperfection. *Adv Mater* **31**, e1902956 (2019).
8. X. Wang *et al.*, Development of an activatable Lysosome-targeted fluorescent probe for the detection of endogenous ONOO(-) levels. *Talanta* **270**, 125581 (2024).
9. M. E. Candela *et al.*, Cryopreserved human alternatively activated macrophages promote resolution of acetaminophen-induced liver injury in mouse. *NPJ Regen Med* **10**, 5 (2025).
10. T. B. Brismar *et al.*, Oral Manganese Chloride Tetrahydrate: A Novel Magnetic Resonance Liver Imaging Agent for Patients With Renal Impairment: Efficacy, Safety, and Clinical Implication. *Invest Radiol* **59**, 197-205 (2024).
11. Y. Wu *et al.*, A mesoporous polydopamine nanoparticle enables highly efficient manganese encapsulation for enhanced MRI-guided photothermal therapy. *Nanoscale* **13**, 6439-6446 (2021).
12. Y. Zheng *et al.*, Evaluation of Reactive Oxygen Species Scavenging of Polydopamine with Different Nanostructures. *Adv Healthc Mater* **13**, e2401816 (2024).
13. M. Zhu *et al.*, Recent developments in mesoporous polydopamine-derived nanoplatforms for cancer theranostics. *J Nanobiotechnology* **19**, 387 (2021).
14. Y. Zhao *et al.*, l-Arginine Alleviates LPS-Induced Oxidative Stress and Apoptosis via Activating SIRT1-AKT-Nrf2 and SIRT1-FOXO3a Signaling Pathways in C2C12 Myotube Cells. *Antioxidants (Basel)* **10** (2021).
15. H. B. Haroon, A. C. Hunter, Z. S. Farhangrazi, S. M. Moghimi, A brief history of long circulating nanoparticles. *Adv Drug Deliv Rev* **188**, 114396 (2022).
16. H. Ao *et al.*, Enhanced tumor accumulation and therapeutic efficacy of liposomal drugs through over-threshold dosing. *J Nanobiotechnology* **20**, 137 (2022).
17. S. Liu *et al.*, MRI-visible mesoporous polydopamine nanoparticles with enhanced antioxidant capacity for osteoarthritis therapy. *Biomaterials* **295**, 122030 (2023).
18. B. K. Wilson, R. K. Prud'homme, Nanoparticle size distribution quantification from transmission

electron microscopy (TEM) of ruthenium tetroxide stained polymeric nanoparticles. *J Colloid Interface Sci* **604**, 208-220 (2021).

19. C. Xu *et al.*, Hepatic neddylation deficiency triggers fatal liver injury via inducing NF-κB-inducing kinase in mice. *Nat Commun* **13**, 7782 (2022).
20. Y. T. Lu *et al.*, Small Extracellular Vesicles Engineered Using Click Chemistry to Express Chimeric Antigen Receptors Show Enhanced Efficacy in Acute Liver Failure. *J Extracell Vesicles* **14**, e70044 (2025).
21. C. Zheng *et al.*, Myocardial cell mitochondria-targeted mesoporous polydopamine nanoparticles eliminate inflammatory damage in cardiovascular disease. *Int J Biol Macromol* **282**, 137141 (2024).
22. T. O. Ajibade *et al.*, L-arginine and lisinopril supplementation protects against sodium fluoride-induced nephrotoxicity and hypertension by suppressing mineralocorticoid receptor and angiotensin-converting enzyme 3 activity. *Environ Sci Pollut Res Int* **30**, 23263-23275 (2023).
23. A. Cui *et al.*, Nitric oxide-mediated the therapeutic properties of induced pluripotent stem cell for paraquat-induced acute lung injury. *Front Immunol* **14**, 1136290 (2023).

Figure captions

Figure1 Physicochemical characterization of MM and AMM nanoparticles

(A) Typical morphology of MM; (B) Typical morphology of AMM; (C) Nitrogen adsorption–desorption isotherm of MM; (D) Pore size distribution curve of MM; (E) Average hydrodynamic diameters of MM and AMM; (F) Zeta potentials of MM and AMM; (G) TGA curves of MM and AMM nanoparticles.

Figure 2 In vitro longitudinal relaxation performance assay of AMM nanoparticles

(A) T1 mapping images of AMM solutions at different concentrations; (B) Fitted curve of the longitudinal relaxivity (r_1) of AMM.

Figure 3 Effect of AMM nanoparticles at different concentrations on the viability of AML12 cells.

Figure 4 Confocal fluorescence images of cellular uptake of AMM nanoparticles by cells at different co-incubation time points.

Figure 5 Quantitative analysis of intracellular AMM fluorescence intensity over time.

Figure 6 Effect of AMM on body weight of rats.

Figure 7 H&E staining images of major organs of rats (40× magnification).

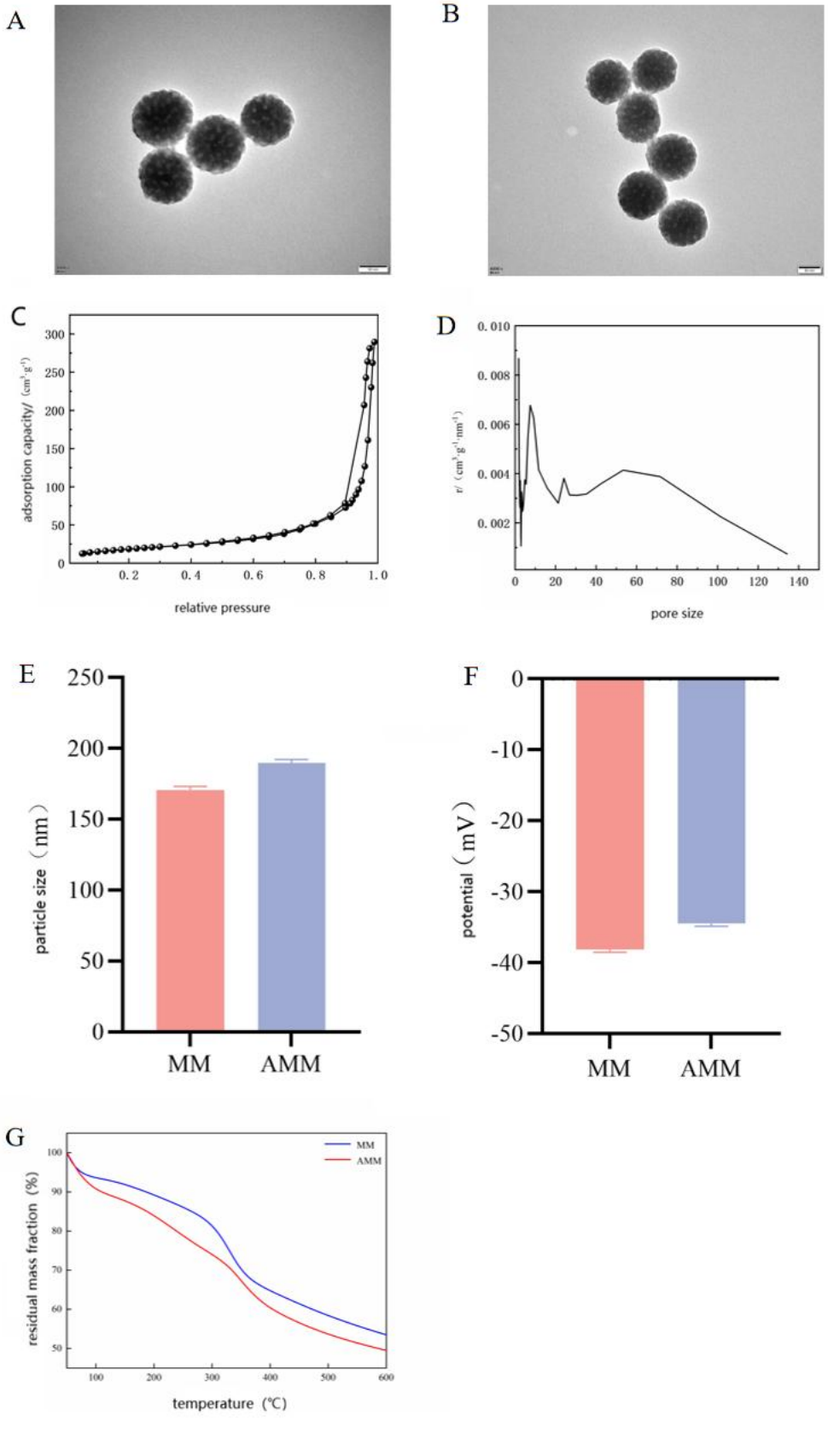
Figure 8 H&E staining images of rat livers in the control group and the model group (10× magnification).

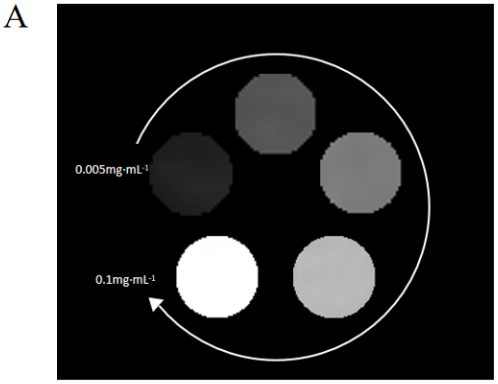
Figure 9 T1 mapping images of rat livers in the control group and the model group at different time points before and after AMM injection.

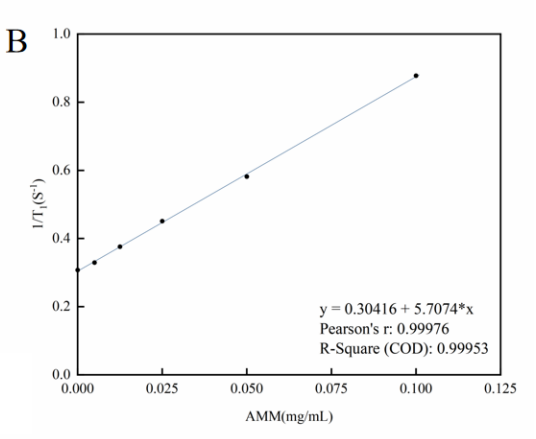
Figure 10 H&E staining images of liver tissues of rats in each group (10× magnification)

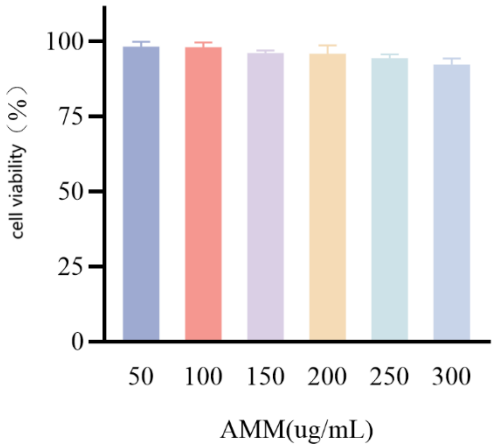
Figure 11 Quantitative analysis of the hepatoprotective effects of AMM on TAA-induced ALI rats

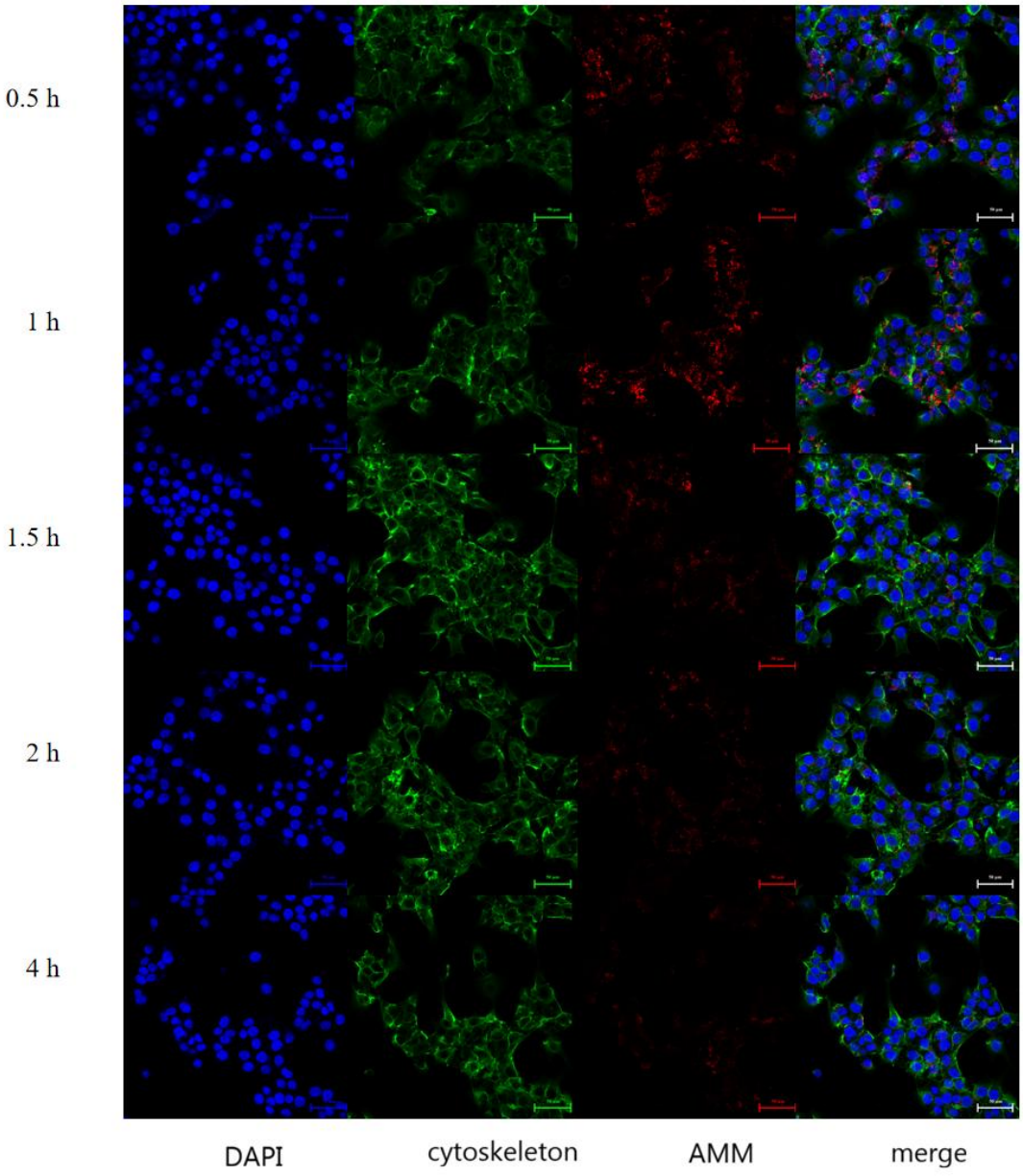
(A) Quantitative statistical results of the percentage of inflammatory area in liver tissues; (B) Detection results of ROS levels in liver tissues; (C) Detection results of serum inflammatory cytokine levels of TNF-α and IL-6; (D) Detection results of serum enzymatic indicators of ALT and AST activities.

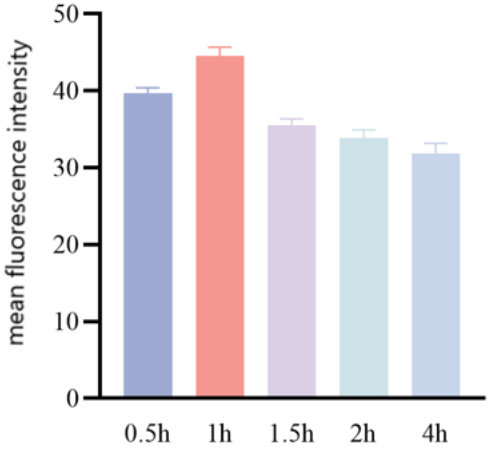

A
B
C
adsorption capacity/ (cm³·g⁻¹)
relative pressure
D
r/ (cm³·g⁻¹·nm⁻¹)
pore size
E
particle size（nm）
MM
AMM
F
potential（mV）
MM
AMM
G
residual mass fraction (%)
temperature (℃)
MM
AMM

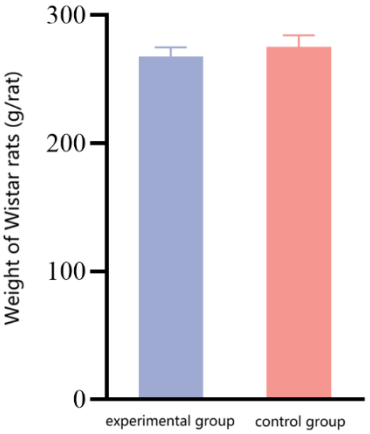

A
0.005mg·mL-1
0.1mg·mL-1

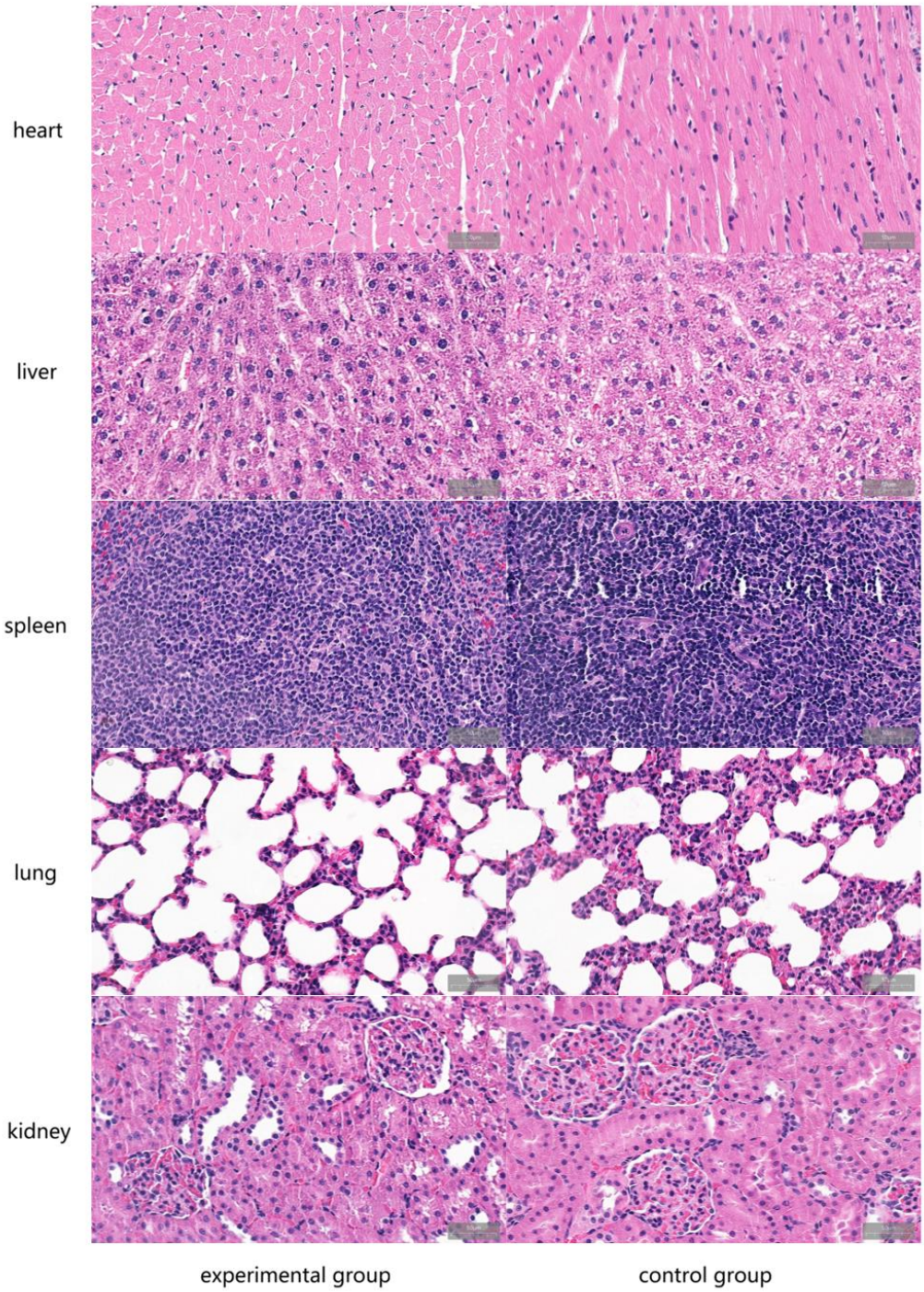

B
1.0
0.8
0.6
0.4
0.2
0.0
1/T1(S-1)
y = 0.30416 + 5.7074*x
Pearson's r: 0.99976
R-Square (COD): 0.99953
0.000
0.025
0.050
0.075
0.100
0.125
AMM(mg/mL)

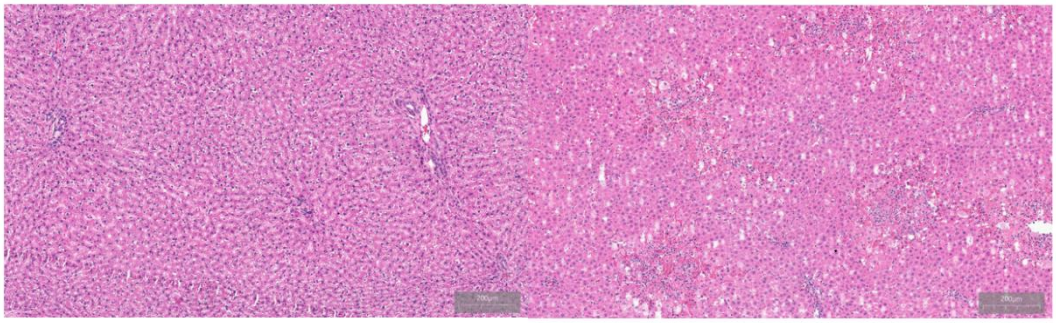

100
75
50
25
0
cell viability（%）
50
100
150
200
250
300
AMM(ug/mL)


0.5 h
1 h
1.5 h
2 h
4 h
DAPI
cytoskeleton
AMM
merge

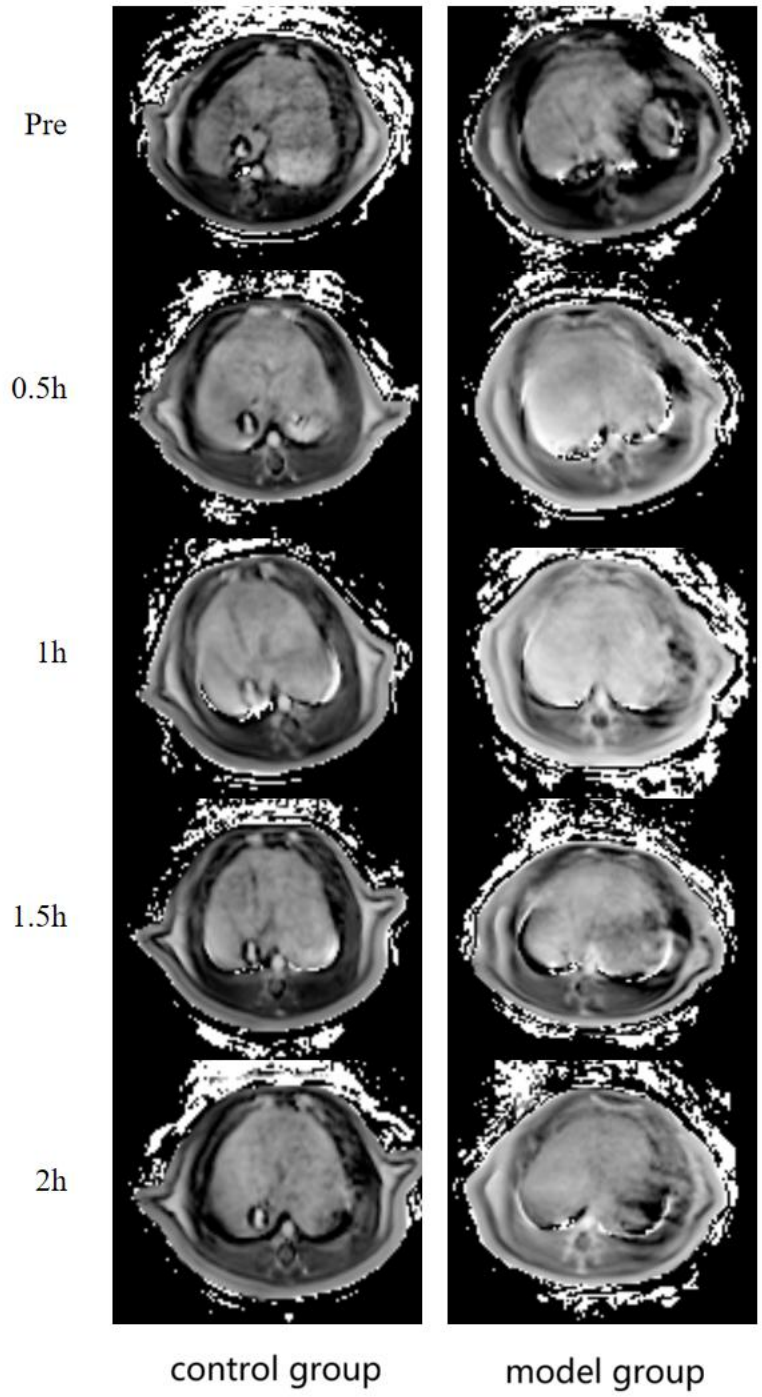

mean fluorescence intensity
50
40
30
20
10
0
0.5h
1h
1.5h
2h
4h

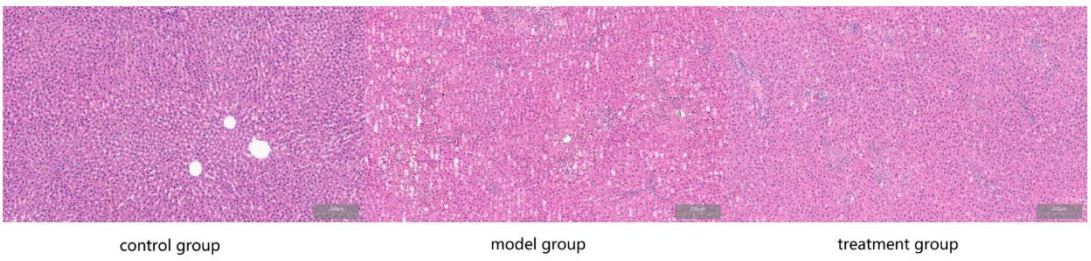

Weight of Wistar rats (g/rat)
300
200
100
0
experimental group
control group

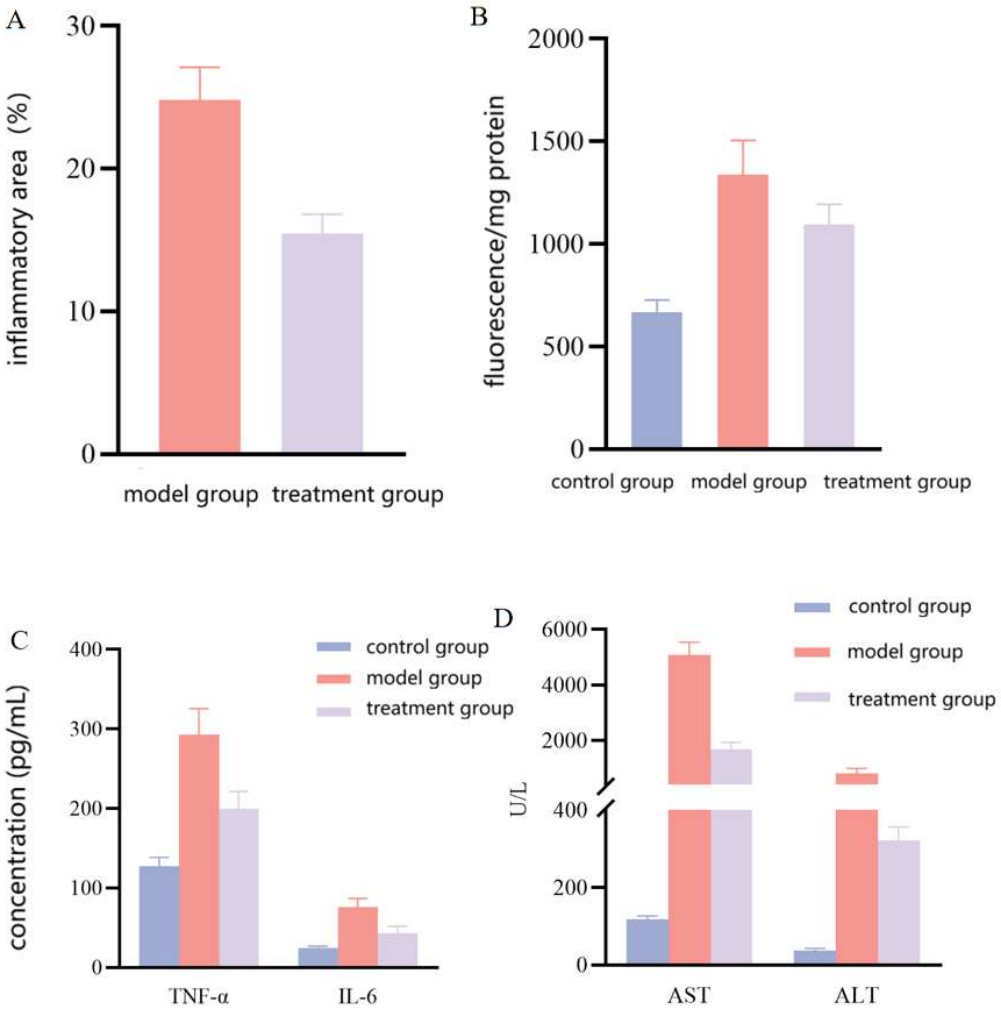

heart
liver
spleen
lung
kidney
experimental group
control group



control group model group


Pre
0.5h
1h
1.5h
2h
control group
model group


control group
model group
treatment group


A
inflammatory area (%)
30
20
10
0
model group
treatment group
B
fluorescence/mg protein
2000
1500
1000
500
0
control group
model group
treatment group
C
concentration (pg/mL)
400
300
200
100
0
control group
model group
treatment group
TNF-α
IL-6
D
U/L
6000
4000
2000
400
200
0
control group
model group
treatment group
AST
ALT